Low-temperature anomalies in muon spin relaxation of solid and hollow γ-Fe_2O_3 nanoparticles: A pathway to detect unusual local spin dynamics

M. Basini,[1,*] S. Sanna,[2,†] T. Orlando,[3,‡] L. Bordonali,[4] M. Cobianchi,[3] P. Arosio,[1] M. Mariani,[3] D. Peddis,[5] V. Bonanni,[1,6] R. Mathieu,[7] T. Kalaivani,[8] G. Singh,[9] J. Larionova,[10] Y. Guari,[10] L. Lartigue,[11] and A. Lascialfari[1,3]

[1]*Dipartimento di Fisica and INSTM, Università degli Studi di Milano, 20133 Milano, Italy*
[2]*Department of Physics and Astronomy "A. Righi," University of Bologna, 40127 Bologna, Italy*
[3]*Dipartimento di Fisica, INFN and INSTM, Università degli Studi di Pavia, 27100 Pavia, Italy*
[4]*Karlsruhe Institute of Technology, Institute of Microstructure Technology, 76344 Eggenstein-Leopoldshafen, Germany*
[5]*Dipartimento di Chimica e Chimica Industriale, Università degli Studi di Genova, 1-16146 Genova, Italy*
[6]*CNR-IOM, Area Science Park, Strada Statale 14 km 163.5, Basovizza 34149, Trieste, Italy*
[7]*Department of Engineering Sciences, Uppsala University, Box 534, SE-751 21 Uppsala, Sweden*
[8]*Bilknet University–UMRAM, Ankara, Turkey*
[9]*School of Biomedical Engineering, The University of Sydney, Sydney, NSW 2008, Australia*
[10]*ICGM, Université Montpellier, CNRS, ENSCM, 34095 Montpellier, France*
[11]*Université de Nantes, CNRS, CEISAM UMR 6230, 44000 Nantes, France*

(Received 1 September 2020; accepted 21 October 2020; published 19 November 2020)

By means of muon spin relaxation measurements we unraveled the temperature spin dynamics in monodisperse maghemite spherical nanoparticles with different surface to volume ratio, in two samples with a full core (diameter $D \sim 4$ and $D \sim 5$ nm) and one with a hollow core (external diameter $D \sim 7.4$ nm). The behavior of the muon longitudinal relaxation rates as a function of temperature allowed us to identify two distinct spin dynamics. The first is well witnessed by the presence of a characteristic peak for all the samples around the so-called muon blocking temperature $T_B^{\mu+}$. A Bloembergen-Purcell-Pound (BPP)-like model reproduces the experimental data around the peak and at higher temperatures ($20 < T < 100$ K) by assuming the Néel reversal time of the magnetization as the dominating correlation time. An additional dynamic emerges in the samples with higher surface to volume ratio, namely, full 4 nm and hollow samples. This is witnessed by a shoulder of the main peak for $T < 20$ K at low longitudinal field ($\mu_0 H \approx 15$ mT), followed by an abrupt increase of the relaxation rate at $T < 10$ K, which is more evident for the hollow sample. These unusual anomalies of the longitudinal relaxation rate for $T < T_B^{\mu+}$ are suggested to be due to the surface spins' dynamical behavior. Furthermore, for weak applied longitudinal magnetic field ($\mu_0 H \approx 15$ mT) and $T < T_B^{\mu+}$ we observed damped coherent oscillations of the muon asymmetry, which are a signature of a quasistatic local field at the muon site as probed by muons implanted in the inner magnetic core of the nanoparticles. The muon spin relaxation technique turns out to be very successful to study the magnetic behavior of maghemite nanoparticles and to detect their unusual local spin dynamics in low magnetic field conditions.

DOI: 10.1103/PhysRevB.102.195424

I. INTRODUCTION

The spin dynamics of confined magnetic materials nowadays is of great interest for both fundamental and applied physics, and its investigation is mainly performed with the intent to correlate all possible physical mechanisms active at the nanoscale to their macroscopic properties. Among the available nanosystems, the spinel iron oxide magnetic nanoparticles (MNPs) have been widely studied with particular attention to the effects of the magnetic core size and the topology [1–6]. The possibility of synthesizing MNPs with a well-defined size and shape boosted their application in several fields such as, e.g., photonics, catalysis, magnetic recording, biological sensing [7], and biomedical theranostics [8,9]. Additionally, MNPs, revealed intriguing fundamental physical phenomena [10–13]. These systems display different thermally activated magnetic phases (superspin glass, ferrimagnetism, superparamagnetism) which result from a balance among the exchange coupling, the surface effects, and the interparticle interactions. The available thermal energy determines the accessible spin dynamics regime. Depending

*Present address: Department of Physics, Stockholm University, 10691 Stockholm, Sweden.
†Corresponding author: s.sanna@unibo.it
‡Present address: Max Planck Institute for Biophysical Chemistry, 37077 Göttingen, Germany.

on temperature and external field, in each regime different correlation times are dominating, such as the Néel magnetization reversal time, the Brownian relaxation time, and so on [14].

The spin dynamics in iron oxide MNPs has been widely investigated over the past 20 years [15–26]. It has been shown that iron oxide MNPs are constituted by a single magnetic domain when the particle diameter is $D < D_c$, where D_c is the critical diameter, which varies between tens and hundreds of nanometers, depending on the material. In this condition, the system displays a superparamagnetic behavior [27]. Measurements of the static macroscopic magnetization show a temperature activated behavior, where the magnetic domains are blocked for temperatures below the so-called blocking temperature, while they are freely orienting at higher temperatures [21,28]. This blockage gives rise to irreversibility effects, which lead to the departure of zero-field-cooled and field-cooled (ZFC-FC) curves and hysteresis opening. When interfaces among two different MNP magnetic phases are present, an exchange bias effect can be experimentally observed [29]. More recently, studies conducted on MNPs with hollow geometry revealed peculiar magnetic properties, such as low blocking temperatures and small magnetic moments. By means of magnetic measurements and semiclassical simulations, this behavior was attributed to a multidomain microstructure [30] and to the non-negligible contribution of the surface spins, which display broken translational symmetry and higher anisotropy than the spins with bulk coordination [31]. However, the magnetic response of MNPs obtained with dc magnetometry, which is sensitive only to slow dynamics (10^{-2}–1 Hz), is a combination of surface and bulk effects that cannot be entirely disentangled [31]. This is further complicated by the fact that, despite an excellent control of the crystallinity and the size distribution [32,33], different synthesis procedures strongly affect the properties and the thickness of the surface spin's corona [34,35].

Techniques such as nuclear magnetic resonance (NMR) and muon spin relaxation (μ^+SR) are suited to investigate the relatively fast local spin dynamics in MNPs, because they are sensitive to higher frequency ranges than those achievable by magnetometry (10^4–10^9 Hz for NMR and 10^5–10^8 Hz for μ^+SR) and provide insights into the local magnetic properties in proximity of the experimental probe (magnetic nucleus for NMR and muon for μ^+SR). For studying an extended range of frequencies, such techniques can be combined to ac susceptometry (range 1–10^4 Hz) [36], Mössbauer (10^8–10^{10} Hz) [37], neutron scattering (10^8–10^{14} Hz) [18], and electron spin resonance (1–100 GHz) [38]. Recently, wideband NMR relaxometry targeting the ^{1}H nuclei of the organic coating of iron oxide MNP powders ($D \sim 3$ nm) allowed for a quantitative analysis of the Néel reversal process [28]. With the same technique, a slower dynamics was detected at low temperatures ($T < 15$ K) in full iron oxide MNPs ($D \sim 7$ nm) and core-shell gold-magnetite nanoparticles which could be ascribed to a complex interplay of surface and bulk spins [36], in agreement with dc magnetometry studies [31].

Unlike other spectroscopic techniques such as nuclear magnetic resonance (NMR), μ^+SR has the advantage to operate also in zero and low applied magnetic fields, thus allowing to distinguish low-energy effects that can be dampened in the presence of high external magnetic fields. Furthermore, the muon can be implanted directly into the ferrite material. However, to our knowledge, only one study reported on μ^+SR in zero field as a function of temperature on maghemite MNPs ($D \sim 9$ nm) [37]. Despite the authors having identified the blocked and the superparamagnetic state, other features, such as the local magnetic field inside the MNPs and surface effects, were not detected, possibly because of the large interparticle dipolar interaction [37] and/or frequency window limits of the experimental technique.

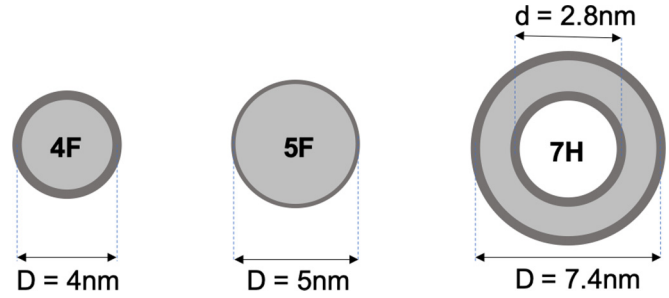

FIG. 1. Schematic drawing of the three investigated samples: from the left 4F, 5F, and 7H. D and d indicate the external and internal diameter, respectively. The light and dark gray indicate the volume occupied by the bulk spins (V_{bulk}) and by the surface spin corona (V_{surf}), respectively.

In this work we perform μ^+SR measurements to investigate three MNP samples of different size and topology, optimally designed to disentangle the spin dynamics of the surface spins and of the bulk ones. We synthesized two samples with full core diameter (4F with $D \sim 4$ nm, and 5F with $D \sim 5$ nm), and one sample with hollow core (7H), having external diameter $D \sim 7.4$ nm and internal diameter $d \sim 2.8$ nm. The longitudinal muon relaxation rate as a function of temperature $\lambda(T)$ shows a broad peak with a maximum at $\sim 25 \div 50$ K attributed to the dynamics of the ferrite spins with bulk coordination. At lower temperatures and low field ($\mu_0 H = 15$ mT) $\lambda(T)$ displays a shoulder followed by an anomalous increase at $T < 10$ K, which is more pronounced in the hollow sample. These low-T anomalies have been attributed to the dynamics of the surface spins, dominated by a correlation time shorter than the one of bulk spins. Interestingly, a highly damped coherent oscillation is observed in the muon decay asymmetry at low temperatures, reflecting the presence of a coherent muon spin precession around a local field arising from the blocked (i.e., locally ordered) phase of the nanoparticles.

II. EXPERIMENTAL DETAILS

Two spherical MNPs with a full iron oxide core and one spherical sample with a hollow core were synthesized (see Fig. 1 for a schematic drawing). Full MNPs have been synthesized using the protocol proposed by Sun *et al.* [39]. MNPs with hollow topology have been synthesized following a well-established procedure based on the Kirkendall effect [40–49]. Iron pentacarbonyl [$Fe(Co)_5$] is decomposed in air-free conditions at around 220 °C in oleylamine and octadecene [41–50]. The resulting iron-based NPs are oxidized at 220 °C in octadecene by means of oleic acid [42,43]. The formation

TABLE I. Morphological parameters (diameter, particle volume V_{tot}, volume occupied by the bulk spins V_{bulk}) and blocking temperatures $T^{SQUID}_{max,ZFC}$ and $T_B^{\mu+}$ measured by low-field magnetometry (SQUID) and muon spin relaxation (μ^+SR) techniques on different samples. Column 6 represent the volume of the surface spin corona (V_{surf}) normalized to the total volume ($V_{tot} = V_{bulk} + V_{surf}$). The surface thickness was previously evaluated by Mössbauer analysis on the same sample [46].

Sample label	Geometry	Diameter (nm)	V_{tot} (nm^3)	V_{bulk} (nm^3)	V_{surf}/V_{tot} (ad.)	$T^{SQUID}_{max,ZFC}$ (K)	$T_B^{\mu+}$ (K)
4F	Full	4.0(0.3)	34(5)	14(4)–24(5)	0.3–0.6	10(1)	28(4)
5F	Full	5.0(0.1)	65(3)	64(2)	0.012	23(2)	46(5)
7H	Hollow	(D) 7.4(0.1) (d) 2.8(0.1)	201(9)	102(6)	0.49	29(2)	40(5)

of hollow nanoparticles is due to the self-diffusion velocity of iron and oxygen ions [40,42,43]. The 4F full sample is coated with a rhamnose derivative while samples 5F and 7H are coated with oleic acid. The coating, together with the small dimensions of our samples, guarantees a partial shielding of the dipolar interparticle interactions [43] and prevents aggregation.

Structural and magnetic characterization, i.e., by x-ray diffraction, high-resolution transmission electron microcopy, and Mössbauer spectroscopy (not reported here), confirmed that all the samples are constituted by iron oxide with spinel cubic structure, mainly maghemite (γ-Fe_2O_3), with absence of Verwey transition. No experimental evidence of tetragonal superstructures, due to ordering of vacancies, has been observed. These data are in excellent agreement with the literature [30,44].

From transmission electron microscopy measurements performed by using a Hitachi S-5500 microscope operating at 30 K, we estimated the inorganic core diameter of the MNPs (for TEM images refer to [43] and Supplemental Material [44]). The diameters D of the samples 4F and 5F were $D = 4.0 \pm 0.3$ nm and $D = 5.0 \pm 0.1$ nm, respectively. The sample 7H has a diameter $d = 2.8 \pm 0.1$ nm for the inner hole and $D = 7.4 \pm 0.1$ nm as outer diameter. The geometrical parameters are summarized in Table I and the materials topology is sketched in Fig. 1.

The static magnetic properties of powder samples were investigated by means of zero-field-cooled (ZFC) and field-cooled (FC) magnetization curves collected on a superconducting quantum interference device (SQUID) magnetometer by Quantum Design, operating in dc mode in the temperature range $2 < T < 300$ K, under applied magnetic fields $\mu_0 H = 20,\ 150$ mT for the sample 4F and $\mu_0 H = 15,\ 120$ mT for the samples 5F and 7H.

The μ^+SR experiments were performed on the GPS beamline of the Swiss Muon Source at the Paul Scherrer Institute (PSI), Villigen (CH). All samples were measured in powders. A 100% spin-polarized positive muon (μ^+) beam is implanted into the sample with the muon spin antiparallel to the muon momentum ($S_\mu = 1/2$). The positive muons are trapped in implantation sites that correspond to minima for the electric potential of the system. The time evolution of the muon asymmetry decay is $A(t) = \frac{N_F - N_B}{N_F + N_B}$, $N_{F,B}$ being the number of emitted positrons counted forward (F) and backward (B) with respect to the initial muon spin polarization. $A(t)$ has been detected as a function of temperature, in the range $1.5\,\text{K} < T < 150\,\text{K}$, and for two applied magnetic fields in the longitudinal geometry, i.e., with the external magnetic field parallel to the initial muon spin polarization. For consistency, we used for each sample the longitudinal field (LF) used for SQUID magnetometry characterization: (i) $\mu_0 H = 20$ mT for sample 4F and 15 mT for samples 7H and 5F, that we refer to as low-field condition, and (ii) $\mu_0 H = 150$ mT for sample 4F and 120 mT for samples 7H and 5F, corresponding to the high-field condition. The total amplitude a_t of the muon asymmetry at $t = 0$ has been estimated at room temperature with an applied magnetic field of 5 mT, transverse with respect to the initial muon spin polarization.

III. RESULTS AND DISCUSSION

A. Dc magnetometry

The magnetization curves collected in low externally applied magnetic field are shown in Fig. 2 (for high field see [43] and Supplemental Material [44] for zero-field-cooling and field-cooling curves). A maximum in the ZFC curve ($T^{SQUID}_{max,ZFC}$) was observed for all samples. This, together with the closed hysteresis observed at room temperature and the open ones measured at low T (see [43] and Supplemental Material [44] for hysteresis loops), classify our systems as superparamagnetic. Furthermore, the overlap of ZFC and FC for $T >$

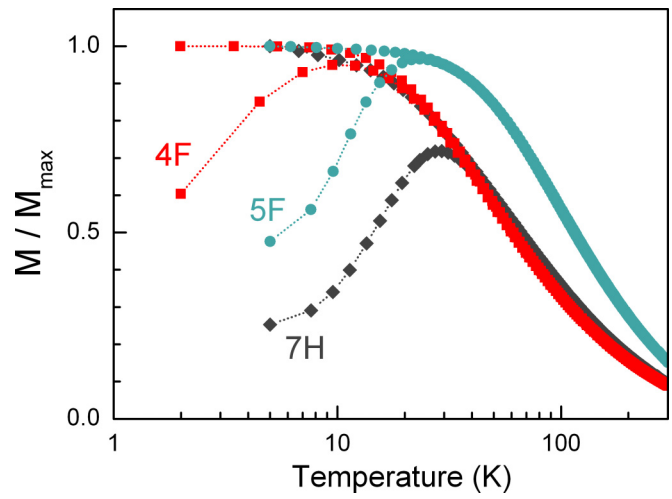

FIG. 2. ZFC and FC magnetization curves as a function of temperature for 4F (diamonds), 5F (squares), and 7H (triangles). The measurements have been performed at $\mu_0 H = 20$ mT (4F sample) and 15 mT (5F and 7H samples). ZFC curves display a maximum at a temperature defined [51] as blocking temperature, $T^{SQUID}_{max,ZFC}$ (reported in Table I).

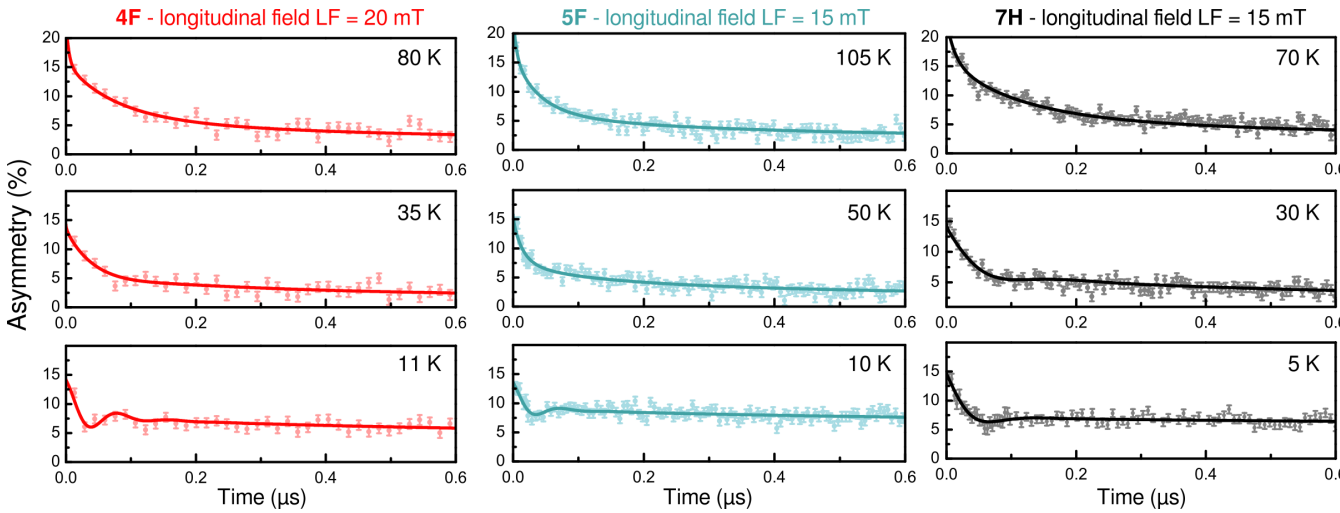

FIG. 3. From left to right: muon asymmetry data for 4F (LF = 20 mT), and 5F and 7H (LF = 15 mT) collected at different temperatures. Solid lines are best fit curves (see text).

$T^{\mathrm{SQUID}}_{\mathrm{max,ZFC}}$ confirms low particle aggregation. The maximum corresponds to the condition $\omega^{\mathrm{SQUID}}_{\mathrm{meas}}\tau_C \sim 1$, where $\nu^{\mathrm{SQUID}}_{\mathrm{meas}} = \omega^{\mathrm{SQUID}}_{\mathrm{meas}}/2\pi$ is the frequency of the experimental measurement and τ_c is a typical correlation time of the electronic system (or an average of a distribution of correlation times). We identify $T^{\mathrm{SQUID}}_{\mathrm{max,ZFC}}$ as the "effective" blocking temperature of the bulk spin system, which is known to be higher than the real average spin blocking T_B temperature, where the correlation time is the Néel reversal time τ_N [47,48,49]. The temperatures $T^{\mathrm{SQUID}}_{\mathrm{max,ZFC}}$ for the different systems are summarized in Table I. The 5F sample shows a $T^{\mathrm{SQUID}}_{\mathrm{max,ZFC}}$ significantly higher than 4F, a scaling expected by considering their core dimensions [50]. The temperature $T^{\mathrm{SQUID}}_{\mathrm{max,ZFC}}$ of 5F and 7H is comparable and in agreement with previous reports [51].

B. Muon spin relaxation

1. Fit of the muon asymmetry

Figure 3 shows a representative data set of the time dependence of the muon asymmetry at selected temperatures for the three samples at low longitudinal fields (15–20 mT). For all three samples, the data indicate two very different behaviors of the experimental muon asymmetry which correspond to two distinct temperature regimes, in the following identified as a frozen (blocked) and a fluctuating spin regime with respect to the μ^+SR experimental timescale.

In the high-temperature regime, above the muon blocking temperature, $T_B^{\mu+}$, the LF muon asymmetry was fitted to the phenomenological equation:

$$A(t) = a_F e^{-\lambda_F t} + a_I e^{-\lambda_I t} + a_S e^{-(\lambda_S t)^{0.5}}. \qquad (1)$$

The presence of three components reflects the existence of at least three inequivalent muon implantation sites with different longitudinal relaxation rates, hereafter λ_{F} (fast relaxation), λ_I (intermediate relaxation), and λ_{S} (slow "stretched" relaxation) with $\lambda_S < \lambda_I < \lambda_F$. The a_F, a_I, and a_S amplitudes of the three components are proportional to the muon population on each inequivalent implantation site. We assume that no change in the population of the implantation sites occurs as a function of temperature, because no structural phase transition is expected. Therefore, the amplitudes are kept as fixed parameters in the fitting function, Eq. (1). The a_F, a_I, and a_S values normalized to the total amplitude a_t are reported in Table II. These amplitudes are sample dependent, reflecting the different sample size and topology.

The slow-relaxing component can be ascribed to muons implanted near to or inside the particle coating, hence experiencing a small coupling with the MNPs magnetic ions. The intermediate- and the fast-relaxing components can be attributed to muons implanted in the ferrite core, either in the surface or bulk, in two different crystallographic implantation sites, the fast component being related to a site closer to the Fe ions.

At low temperature, i.e., below $T_B^{\mu+}$, $A(t)$ displays a severe reduction of the total signal amplitude a_t. The missing fraction nearly coincides with the relative amplitude of the fast component a_F/a_t. This indicates that in this low-T regime the component with the fastest rate exceeds the experimen-

TABLE II. Amplitudes of the different components of the muon asymmetry, normalized to the total amplitude a_t measured at room temperature, below and above the muon blocking temperature $T_B^{\mu+}$.

Sample	$T < T_B^{\mu+}$	$T > T_B^{\mu+}$
4F	$\frac{a_I}{a_t} = 0.25(2)$	$\frac{a_F}{a_t} = 0.39(2)$
	$\frac{a_{I,L}}{a_t} = 0.12(1)$	$\frac{a_I}{a_t} = 0.37(3)$
	$\frac{a_S}{a_t} = 0.24(2)$	$\frac{a_S}{a_t} = 0.24(1)$
5F	$\frac{a_{I,T}}{a_t} = 0.20(2)$	$\frac{a_F}{a_t} = 0.50(3)$
	$\frac{a_{I,L}}{a_t} = 0.10(1)$	$\frac{a_I}{a_t} = 0.30(2)$
	$\frac{a_S}{a_t} = 0.20(1)$	$\frac{a_S}{a_t} = 0.20(1)$
7H	$\frac{a_{I,T}}{a_t} = 0.25(2)$	$\frac{a_F}{a_t} = 0.37(2)$
	$\frac{a_{I,L}}{a_t} = 0.13(1)$	$\frac{a_I}{a_t} = 0.38(2)$
	$\frac{a_S}{a_t} = 0.25(2)$	$\frac{a_S}{a_t} = 0.25(1)$

tal time window (of the order of $100\,\mu s^{-1}$), and becomes undetectable. Furthermore, well below $T_B^{\mu+}$ the data show a damped oscillation of the asymmetry in all the samples (see Fig. 3, low-temperature curves), whose frequency is found to increase as the temperature decreases. According to the above considerations, the total muon asymmetry below $T_B^{\mu+}$ has been fitted to the following three-component function:

$$A(T) = a_{I,L}e^{-\lambda_{I,L}t} + a_{I,T}\cos(\gamma_\mu B_{\rm loc}t)e^{-\lambda_{I,T}t} + a_S e^{-(\lambda_S t)^{0.5}}. \quad (2)$$

For geometrical reasons that will be explained in the next section, in powder samples and low fields one has $a_{I,T} = \frac{2}{3}a_I$ and $a_{I,L} = \frac{1}{3}a_I$. a_S and a_I are constant over the whole temperature range and have the same values used in Eq. (1) at $T > T_B^{\mu+}$ (Table I). In Eq. (2) $\lambda_{I,L}$ represents the longitudinal relaxation rate below $T_B^{\mu+}$ [equivalent to λ_I of Eq. (1)], while $\lambda_{I,T}$ is the very fast transversal rate ($\lambda_{I,T} \gg \lambda_{I,L}$) that damps the oscillation. The weights of different components included in the fitting functions of Eqs. (1) and (2) have been determined with accurate comparisons among raw data collected at low, intermediate, and high temperatures, at the two applied fields.

The experimental behavior of the total asymmetry at low T as a function of time is reported in Fig. 3 for low field and representative temperatures, together with the fitting curves obtained by using Eqs. (1) or (2) above and below $T_B^{\mu+}$, respectively. At high-field condition the oscillation is completely lost (not shown) and the fitting curves are the same as those of Eqs. (1) and (2) by setting the cosine factor to 1.

2. Longitudinal muon relaxation rate

The longitudinal relaxation rates $\lambda_F, \lambda_I, \lambda_s$ of Eqs. (1) and (2) describe the spin-lattice relaxation rate of the muon spins implanted in different sites. These relaxation rates are strongly influenced by the (electron) spin dynamics of the MNPs through the hyperfine muon-electron coupling. In the weak collision approach, where the hyperfine muon-electron interaction is treated as a perturbation, it can be demonstrated that the field expression for the longitudinal relaxation rate turns out to be [52,53]

$$\lambda(T) \propto \chi T J(\omega_L), \quad (3)$$

where χ is the magnetic susceptibility, χT is a quantity proportional to the average of the squared effective magnetic moment, and $J(\omega_L)$ is the spectral density of the electronic spin fluctuations at the Larmor (muon) frequency ω_L.

Among the different relaxation rates in Eqs. (1) and (2), we will focus on the longitudinal relaxation rate of the intermediate component that is detectable over the whole temperature range. As already mentioned, this relaxation has been indicated as λ_I and $\lambda_{I,L}$ for temperatures above and below $T_B^{\mu+}$, in Eqs. (1) and (2), respectively; hereafter we will refer to it as $\lambda_{\rm Int}$. It should be remarked that the slow longitudinal relaxation rate λ_S displays a qualitatively similar behavior vs temperature and field but, due to its small amplitude, the associated high relative error (for $T > 50$ K, often above 25%) does not allow for further detailed analysis and it is not shown here. To study the spin dynamics, now we focus on the dynamical part of the relaxation rate, i.e., the spectral density $J(\omega)$ of Eq. (3), and discuss $\lambda_{\rm int}$ renormalized by the effective magnetic moment χT, where χT has been evaluated by SQUID experimental data of Fig. 2. The curves $\lambda_{\rm Int}/\chi T$ will be analyzed as a function of temperature at two different longitudinal fields. Three general features can be evinced. First, in the low-field condition (LF = 15 and 20 mT) $\lambda_{\rm Int}/\chi T$ vs T shows a major peak at $T = 28(4)$ K for 4F, $T = 46(5)$ K for 5F, and $T = 40(5)$ K for 7H, whose intensity decreases by increasing the applied field. Secondly, a shoulder is observed at lower temperatures in 4F, 7H, and, to a minor extent, 5F. As a third feature, below 10 K and at the lowest applied field $\lambda_{\rm Int}/\chi T$ increases considerably for 7H and slightly for 5F.

To discuss the temperature behavior of $\lambda_{\rm Int}/\chi T$ we recall that a maximum of the spin-lattice relaxation rate is expected when $\omega_0\tau_c \approx 1$, ω_0 being the frequency of the measuring probe and τ_c the correlation time of a dynamics occurring in the system. In our case, the frequency ω_0 of the probe is the muon Larmor frequency, ω_L, and the electronic correlation time is related to the frequency of the spin fluctuations v_c by the formula $\tau_c = \frac{1}{v_c}$. In our system, assumed to be composed of independent MNPs, the dominating correlation times are (i) the Néel reversal time of the single particle magnetization, $\tau_N = 1/v_N$, (ii) the surface spin's flipping time, $\tau_S = 1/v_S$, and (iii) the Brownian rotational time ($\tau_{\rm BR} = 1/v_{\rm BR}$) of the organic groups (mainly CH_2 belonging to the oleic acid coating). Typically for MNPs with size comparable to the ones here investigated, one can assume $v_{\rm BR} < v_N < v_S$ [54]. Considering that in our experiment the Larmor frequency is $\omega_L \sim 10^7$–10^8 rad/s ($\omega_L \equiv \gamma\mu_0 H$, with $\gamma_\mu/2\pi = 135.54$ MHz/T), the condition $\omega_L\tau_{\rm BR} \sim 1$ occurs typically outside our temperature range of investigation, i.e., at $T > 150$ K (Ref. [36] and references therein), while for the surface spin's freezing dynamics the resonant condition $\omega_L\tau_S \sim 1$ is expected at low temperature [36]. Thus, we may safely assign the main peak observed in Fig. 4 to the Néel spin blockage. Consequently, we define the temperature of the peak as the muon blocking temperature $T_B^{\mu+}$ (where $\omega_L\tau_N \approx 1$). Below $T_B^{\mu+}$ the frequency of the fluctuations of the Fe bulk spins is lower than the muon Larmor frequency, an occurrence that corresponds to the slow-motion regime. On the other side, well above $T_B^{\mu+}$ the Fe spin dynamics approaches the limit of fast motion. As expected, since $v_c = \omega_L/2\pi$ of μ^+SR is much higher than the characteristic frequency of the dc magnetometry, experimentally we observe that $T_B^{\mu+} > T_{\rm max,ZFC}^{\rm SQUID}$ (see Fig. 2, Table I, and Fig. 4).

In the $\lambda_{\rm Int}$ vs T curves, the bulk spin dynamics related to τ_N can be analyzed by using a Bloembergen-Purcell-Pound (BPP)-like model, following previous studies of the NMR and μ^+SR spin-lattice relaxation rate for molecular nanomagnets [55] and magnetic nanoparticles [28,36].

Considering that the Néel reversal flipping is a thermally activated process, we assume an Arrhenius dependence for the correlation time, $\tau_N = \tau_0 e^{\frac{E}{kT}}$, E being the energy barrier of the superparamagnetic system. This expression is valid for noninteracting NPs, a condition roughly fulfilled in our "small" systems. Due to the log-normal distribution of the core size of the particles [43,46] and to the existence of a disordered surface layer, a single energy barrier would be too rough an approximation while a distribution of energy barriers can better describe the results. We assumed a log-normal

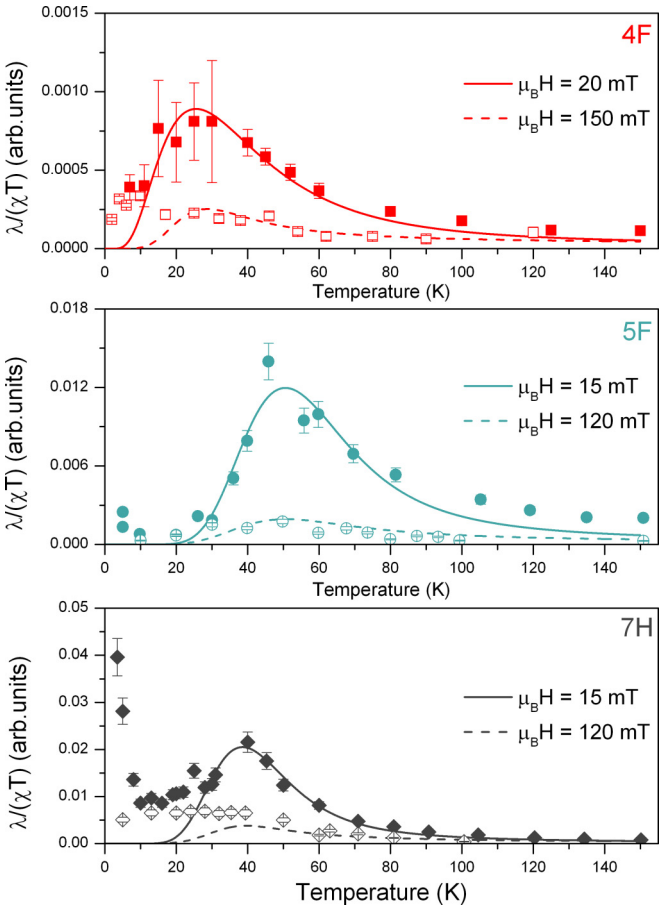

FIG. 4. Temperature dependence of the muon longitudinal relaxation rate $\lambda_{\rm Int}$ renormalized by the effective magnetic moment χT, for all the investigated samples, at two different applied longitudinal fields. The continuous lines represent the best fit to Eq. (5). $\lambda_{\rm Int}$ corresponds to the longitudinal relaxation rates λ_I for $T > T_B^{\mu+}$ and $\lambda_{I,L}$ for $T < T_B^{\mu+}$ of Eqs. (1) and (2), respectively (see text for details).

distribution $P(E)$ of energy barriers E, with median value Δ_N and scale parameter σ (linked to the distribution skewness). With these assumptions the BPP law can be rewritten as

$$(T) = A\chi(T)T \int_0^{+\infty} P(E) \frac{\tau_N\,(T,E)}{1+\tau_N^2(T,E)\omega_L^2} dE, \qquad (4)$$

where $P(E) = \frac{1}{E\sigma\sqrt{2\pi}} \exp[-\frac{\ln(E)-\ln(\Delta_N)}{2\sigma^2}]$ is the log-normal distribution and A is the hyperfine constant. In Table III we summarize all the parameters' values obtained from the fit of $\lambda_{\rm Int}(T)$ by means of Eq. (4) for applied magnetic fields LF = 15/20 mT and 120/150 mT.

The fit of the experimental data to Eq. (4) (solid lines in Fig. 4) well reproduce the peak corresponding to the blocking temperature. Furthermore, one can note that:

(i) The blocking temperature $T_B^{\mu+}$ is systematically higher than $T_{\rm max,ZFC}^{\rm SQUID}$ determined by SQUID magnetometry (Table I), as mentioned above. The values of $T_B^{\mu+}$ measured in our MNPs are consistent with the values reported in the literature, and lower than the blocking temperature measured for MNPs with higher mean diameter, ∼9 nm [37], and also lower than the blocking temperature determined on the sample with mean diameter ∼7 nm from NMR measurements (i.e., with a higher investigation frequency than μ^+SR experiments [36]).

TABLE III. List of parameters obtained from the fit of $\lambda_{\rm Int}(T)$ experimental data reported in Fig. 4. Columns starting from the left: sample, longitudinal field, correlation time for infinite temperature τ_0, median value of the anisotropy barrier Δ_N and scale parameter σ.

Sample	Field (mT)	$\tau_0(10^{-9}$ s)	Δ_N (K)	σ (K)
4F	20	0.26(4)	150(1)	80(3)
5F	15	0.2 (1)	300(30)	60 (20)
7H	15	0.13(2)	250 (60)	50 (30)
4F	150	0.35(6)	87(2)	18(1)
5F	120	0.18(4)	180 (20)	30 (10)
7H	120	0.25(5)	140 (80)	10(2)

(ii) As concerns the decrease of Δ_N with increasing the field, we attribute this behavior to the well-known energy barrier reduction induced by the applied magnetic field [28,36].

(iii) The energy barriers scale with the size of the bulk volume for full samples, being $\frac{\Delta_N(4F)}{k_B} = 150(1)$ K and $\frac{\Delta_N(5F)}{k_B} = 300(30)$ K at low field. The hollow compound, despite the much higher bulk superparamagnetic volume with respect to 5F, within the error presents a comparable barrier $\frac{\Delta_N(7H)}{k_B} = 250(60)$ K, reflecting the presence of smaller multiple crystallographic domains.

(iv) The τ_0 values for all samples are in the typical superparamagnetic range ($10^{-10} \div 10^{-9}$ s). Their field dependence cannot be easily explained, although many experimental and theoretical studies [28] often evidenced such a dependence as well as the variation of τ_0 when local (NMR, neutron scattering, Mössbauer, μ^+SR) or macroscopic ($\chi_{\rm dc}$, $\chi_{\rm ac}$) techniques are used.

(v) Although the bulk volume of the hollow 7H sample is higher than the volume of the full 5F sample, their $T_B^{\mu+}$ are comparable within the experimental error, in apparent contradiction with the typical superparamagnetic behavior. It should, however, be noted that the hollow samples are suggested to have different subdomains in the bulky part [30], thus lowering $T_B^{\mu+}$ [30,31]. In this respect one should consider that μ^+SR is a local technique and, as such, more sensitive to local rearrangement and dynamics of electronic spins, an occurrence that justifies the previous observations.

We now focus on the most relevant outcome of this work: the two additional low-temperature anomalies of $\lambda_{\rm Int}(T)$ (see Fig. 4). The first anomaly is the presence of the shoulder for $T < T_B^{\mu+}$ visible in the 4F and 7H samples and not appreciably in 5F. The fact that the surface to volume ratio (Table I) is small in the 5F ($V_{\rm surf}/V_{\rm tot} \sim$ few percent) and very large in the 4F and 7H samples ($V_{\rm surf}/V_{\rm tot} \sim 50\%$) indicates that this "shoulder" anomaly is related to the dynamics of the surface spin. The second anomaly is the steep increase of $\lambda_{\rm Int}(T)$ observed at the lowest field for $T < 10$ K very remarkably in 7H. The presence of this anomaly in $\lambda_{\rm Int}/\chi T$, a quantity proportional to the dynamical spectral density $J(\omega)$, Eq. (3), might be tentatively attributed again to the surface spin dynamics. The lack of this increase for the 4F sample, despite its large $V_{\rm surf}/V_{\rm tot}$ ratio, might be justified by presuming that

all the spin dynamics are shifted towards low temperature similarly to its $T_B^{\mu+}$, hence pushing the anomaly increase below the lower-temperature limit of the currently investigated range (1.5 K). Interestingly the anomaly increase is almost negligible in 5F, despite its highest $T_B^{\mu+}$, thus supporting the idea that it is related to the surface spin, of which there are relatively few in this sample.

We suggest that the shoulder and the increase are part of the same anomaly possibly occurring in the form of a maximum/peak at temperatures below 1.5 K with a nonstandard BPP Lorentzian profile. An irregular peak profile might be attributed to the expected more complex energy landscape of the surface spin dynamics with irregularly distributed barriers and multiple minima [31].

Qualitatively, the experimental observation that these anomalies occur at temperature $T < T_B^{\mu+}$, related to the bulk spin dynamics, indicates that the dynamics of the surface spins is faster than that of the bulk spins, in agreement with previous magnetic susceptibility measurements for samples of dimensions similar to ours [30,31]. However, the theoretical modeling of such surface spin dynamics is still not available and not universally accepted in the literature [31], and its assessment is well beyond the scope of this work.

3. Local magnetic field

The damped oscillations occurring for $T \ll T_B^{\mu+}$ (see Fig. 3, low-temperature data) and accounted for by the oscillating term in Eq. (2) reflect a coherent precession of the muons' polarization around a local field at the muon site $B_{\rm loc}$, occurring at the Larmor frequency $\omega_L^{\rm loc} \equiv \gamma_\mu B_{\rm loc}$ (with $\gamma_\mu/2\pi = 135.54$ MHz/T). Interestingly, a coherent muon precession has never been reported for MNPs, although it is expected in the case of high crystallinity [37]. In fact, only cases of Kubo-Toyabe behavior, corresponding to a quite large distribution of local fields centered around zero, were reported in the literature [32,37,56]. In superparamagnets (like our systems), generally the local fields are induced by the progressive electronic spin freezing below the blocking temperature, i.e., in the slow spin motion regime. In our samples the damped oscillations reflect a distribution of muon local field with a finite mean intensity value of the order of $B_{\rm loc} \sim$ 50–100 mT at low T, whose second moment distribution is determined by the damping of the oscillating amplitude, $\Delta B_{\rm loc} \approx \lambda_{I,T}/\gamma_\mu \sim$ 10–30 mT. It seems reasonable, and in agreement with the analysis of the whole data set, to assign the oscillating amplitude to those muons which at high temperature $T > T_B^{\mu+}$ give rise to the asymmetry component with the intermediate relaxation time, with amplitude a_I in Eq. (1). Furthermore it should be noted that in powder samples (our case), in the case of frozen magnetic moments (well below $T_B^{\mu+}$), we expect a nearly isotropic distribution of the directions of the internal field $B_{\rm loc}$ at the muon sites both in zero or low applied field. Hence simple geometrical arguments predict that on average 2/3 of the muon spin component is perpendicular to the internal field $B_{\rm loc}$, with the muon polarization precessing with $\omega_L^{\rm loc}$, and 1/3 of it is parallel to $B_{\rm loc}$ (no precession). For this reason we expect that below $T_B^{\mu+}$ the a_I component splits into two subcomponents, labeled as transverse $a_{I,T}$ (oscillating) and longitudinal $a_{I,L}$ (not oscillating) in Eq. (2), with a fraction nearly equal to 2/3 and 1/3 of a_I, respectively. The fitted relative weights of a_I, $a_{I,T}$, $a_{I,L}$ reported in Table II are nicely consistent with the expected behavior for all the samples, confirming the validity of these considerations. The oscillation is typically lost above 10 K because of overdamped oscillations and the cosine term of Eq. (2) can be set to 1.

At a first approximation, the amplitude of $B_{\rm loc}$ is mainly due to the dipolar interaction between the muon spin and the Fe ordered moments, which is proportional to the order parameter of the blocked state, i.e., to the average local (electronic) magnetization$M$. This implies that $B_{\rm loc}$ directly reflects the behavior of the macroscopic (or subdomain) magnetization of the blocked state [30,43]. $B_{\rm loc}$ in the limit of low T is about 100 and 50 mT for the 7H and 5F samples. The fact that 7H displays lower $B_{\rm loc}$ than 5F is in qualitative agreement with the dc magnetization measurements which show a lower macroscopic magnetization in the hollow sample 7H [43]; also see the Supplemental Material [44]. Considering that the size of the magnetic order parameter is expected to increase when the particle volume increases, the observed behavior is apparently inconsistent with the fact that the sample 7H has a higher nominal magnetic bulk volume compared to the sample 5F (see Table I). However, due to the existence of subdomains in hollow samples [30,31], the local field in 7H is expected to be lower.

IV. CONCLUSIONS

By means of low-field μ^+SR, we investigated the spin dynamics of superparamagnetic maghemite-based full and hollow magnetic nanoparticles. For all the samples, the muon asymmetry showed a three-component behavior characterized by longitudinal relaxation rates $\lambda_F > \lambda_I > \lambda_s$—respectively, fast, intermediate, and slow—associated to different implantation sites. The fastest component, corresponding to muons implanted closely to the Fe ions, becomes undetectable at low temperatures ($T <$ 30–50 K) as it falls outside the instrument frequency window. The intermediate- and the slow-relaxation rates display a peak with a maximum at the muon blocking temperature whose values $T_{\rm B}^{\mu+}$ are reported in Table I. This peak appears at the resonance condition $\omega_L \tau_N \approx 1$, where τ_N represents the Néel correlation time of the superparamagnetic dynamics and ω_L as the muon Larmor frequency. Such dynamics is well described by a Bloembergen-Purcell-Pound model in a temperature region around $T_B^{\mu+}$, by assuming a distribution of Arrhenius energy barriers, centered at Δ_N. The energy barriers scale with the size of the bulk volume for full samples. The hollow sample displays an energy barrier comparable to the one of 5F, despite the different bulk superparamagnetic volume, reflecting the presence of smaller multiple crystallographic domains typically expected in hollow samples. These results, obtained through the use of a local probe (muon), are in agreement with the experimental observations and theoretical predictions obtained by experimental data of macroscopic techniques [30,31,57–60]. In addition, for $T < T_B^{\mu+}$ we observed an anomalous behavior of λ (T): A shoulder appears on the left of the BPP peak followed by an increase when temperatures are further lowered below $T \sim$ 10 K, remarkably for the hollow sample. By considering the surface to volume ratio of the

samples under investigation we attribute these experimental anomalies to the dynamics of the surface spins. In fact, upon cooling the surface spins start to freeze when T is decreased below the blocking temperature of the bulk spins, and λ vs T behavior reflects their faster spin dynamics. Finally, we detected the presence of a coherent oscillation due to muons in the inner shell with the intermediate relaxing component λ_I of the muon asymmetry for $T < T_B^{\mu+}$. This oscillation reflects the precession of the muon spin around a local field at the muon site due to a collective spin freezing phenomenon, predicted in literature but never observed before. The inequality $B_{\rm loc}(7{\rm H}) < B_{\rm loc}(5{\rm F})$ strengthens the hypothesis about the existence of a multidomain structure in the hollow sample [30].

We demonstrated that by means of μ^+SR one could single out the local characteristics of magnetic phases and spin dynamics in magnetic nanoparticles and surface and bulk spin dynamics can be distinguished. Future NMR and μ^+SR experiments are currently planned to unravel the details of the unusual local spin dynamics for very low $T < 1.5$ K.

ACKNOWLEDGMENTS

EU COST project Radiomag (Project No. TD-1402) and Eurelax (Project No. CA15209) are gratefully acknowledged. Cariplo Foundation, project BATMAN, and Consorzio INSTM for MOTOSPORT project, are acknowledged as well. This work is based on experiments performed at the Swiss Muon Source SμS, Paul Scherrer Institute, Villigen, Switzerland. The authors are grateful to H. Luetkens; we acknowledge in particular C. Baines and A. Amato for the support during the measurements.

[1] D. A. GaraninPhys. Rev. B **98**, 054427 (2018).
[2] T. P. Choy, J. M. Edge, A. R. Akhmerov, and C. W. J. Beenakker, Phys. Rev. B. **84**, 195442 (2011).
[3] A. Sundaresan, R. Bhargavi, N. Rangarajan, U. Siddesh, and C. N. R. Rao, Phys. Rev. B **74**, 161306(R) (2006).
[4] L. Gragnaniello, T. Ma, G. Barcaro, L. Sementa, F. R. Negreiros, A. Fortunelli, S. Surnev, and F. P. Netzer, Phys. Rev. Lett. **108**, 195507 (2012).
[5] R. H. Kodama and A. E. Berkowitz, Phys. Rev. B **59**, 6321 (1999).
[6] M. M. van Oene, L. E. Dickinson, F. Pedaci, M. Köber, D. Dulin, J. Lipfert, and N. H. Dekker, Phys. Rev. Lett. **114**, 218301 (2015).
[7] G. Schmid, See, e.g., *Nanoparticles: From Theory to Application* (Wiley-VCH, Weinheim, 2004); K. J. Klabunde, *Nanoscale Materials in Chemistry* (Wiley-Interscience, New York, 2001); M. P. Pileni, Nat. Mater. **2**, 145 (2003).
[8] See, e.g., V. V. Mody, A. Cox, S. Shah, A. Singh, W. Bevins, and H. Parihar, Appl. Nanosci **4**, 385 (2014); A. Malik, T. Tahir Butt, S. Zahid, F. Zahid, S. Waquar, M. Rasool, M. Husain Qazi, and A. Mahmood Qazi, J. Nanotechnol. **2017**, 1098765 (2017); P. M. Price, W. E. Mahmoud, A. A. Al-Ghamdi, and L. M. Bronstein, Front. Chem. **6**, 619 (2018); Y. Piñeiro, M. González Gómez, L. de Castro Alves, A. Arnosa Prieto, P. García Acevedo, R. Seco Gudiña, J. Puig, C. Teijeiro, S. Yáñez Vilar, and J. Rivas, Magnetochemistry **6**, 4 (2020).
[9] S. Laurent, D. Forge, M. Port, A. Roch, C. Robic, L. Vander Elst, and R. N. Muller, Chem. Rev. **108**, 2064 (2008).
[10] A. Fraile Rodríguez, A. Kleibert, J. Bansmann, A. Voitkans, L. J. Heyderman, and F. Nolting, Phys. Rev. Lett. **104**, 127201 (2010).
[11] T. V. Lyutyy, S. I. Denisov, A. Y. Peletskyi, and C. Binns, Phys. Rev. B **91**, 054425 (2015).
[12] A. Ghazali and J.-C. Lévy, Phys. Rev. B **67**, 064409 (2003).
[13] L. H. F. Andrade, A. Laraoui, M. Vomir, D. Muller, J.-P. Stoquert, C. Estourne's, E. Beaurepaire, and J.-Y. Bigot, Phys. Rev. Lett. **97**, 127401 (2006).
[14] See, e.g., V. K. Varadan, L. Chen, and J. Xie, *Nanomedicine—Design and Applications of Magnetic Nanomaterials, Nanosensors and Nanosystems* (J. Wiley and Sons, New York, 2008).
[15] K. Komatsu, D. L'Hôte, S. Nakamae, V. Mosser, M. Konczykowski, E. Dubois, V. Dupuis, and R. Perzynski, Phys. Rev. Lett. **106**, 150603 (2011).
[16] J. Tejada, R. D. Zysler, E. Molins, and E. M. Chudnovsky, Phys. Rev. Lett. **104**, 027202 (2010).
[17] A. Sukhov and J. Berakdar, Phys. Rev. Lett. **102**, 057204 (2009).
[18] F. Gazeau, E. Dubois, M. Hennion, R. Perzynski, and Yu. Raikher, Europhys. Lett. **40**, 575 (1997).
[19] T. Hyeon, S. S. Lee, J. Park, and Y. Chung, and H. B. Na, J. Am. Chem. Soc. **123**, 12798 (2001).
[20] S. A. Shah, D. B. Reeves, R. M. Ferguson, J. B. Weaver, and K. M. Krishnan, Phys. Rev. B **92**, 094438 (2015).
[21] M. Basini, T. Orlando, P. Arosio, M. F. Casula, D. Espa, S. Murgia, C. Sangregorio, C. Innocenti, and A. Lascialfari, J. Chem. Phys **146**, 034703 (2017).
[22] P. Arosio, M. Basini, A. Barbaglia, R. Piñol, J. L. Murillo, A. Millán, and A. Lascialfari, J. Nanosci. Nanotechnol. **19**, 2950 (2019).
[23] P. Saha, R. Rakshit, M. Alam, and K. Mandal, Phys. Rev. Appl. **11**, 024059 (2019).
[24] R. Moreno, S. Poyser, D. Meilak, A. Meo, S. Jenkins, V. K. Lazarov, G. Vallejo-Fernandez, S. Majetich, and R. F. L. Evans, Sci. Rep. **10**, 2722 (2020).
[25] A. Kovács, K. Sato, V. K. Lazarov, P. L. Galindo, and T. J. Konno, and Y. Hirotsu, Phys. Rev. Lett **103**, 115703 (2009).
[26] P. Guardia, B. Batlle-Brugal, A. G. Roca, O. Iglesias, M. P. Morales, C. J. Serna, A. Labarta, and X. Batlle, J. Magn. Magn. Mater. **316**, e756 (2007).
[27] J. Frenkel and J. Doefman, Nature **126**, 274 (1930).
[28] L. Bordonali, Y. Furukawa, M. Kraken, F. J. Litterst, C. Sangregorio, M. F. Casula, and A. Lascialfari, Phys. Rev. B **85**, 174426 (2012).
[29] M.-H. Phan, J. Alonso, H. Khurshid, P. Lampen-Kelley, S. Chandra, K. S. Repa, Z. Nemati, R. Das, Ó. Iglesias, and H. Srikanth, Nanomaterials **6**, 221 (2016).

[30] A. Cabot, A. P. Alivisatos, V. P. Puntes, L. Balcells, O. Iglesias, and A. Labarta, Phys. Rev. B **79**, 094419 (2009).
[31] H. Khurshid, P. L. Kelley, Ò. Iglesias, J. Alonso, M. H. Phan, C. J. Sun, M. L. Saboungi, and H. Srikanth, Sci. Rep. **5**, 15054 (2015).
[32] D. Thapa, V. R. Palkar, M. B. Kurup, and S. K. Malik, Properties of magnetite nanoparticles synthesized through a novel chemical route, Mater. Lett. **58**, 2692 (2004).
[33] Q. Li, C. W. Kartikowati, S. Horie, T. Ogi, T. Iwaki, and K. Okuyama, Sci. Rep. **7**, 9894 (2017); M. S. Andersson, R. Mathieu, P. S. Normile, S. S. Lee, G. Singh, P. Nordblad, and J. A. De Toro, Phys. Rev. B **95**, 184431 (2017).
[34] T. N. Shendruk, R. D. Desautels, B. W. Southern, and J. van Lierop, Nanotechnology **18**, 455704 (2007).
[35] D. S. Negi, H. Sharona, U. Bhat, S. Palchoudhury, A. Gupta, and R. Datta, Phys. Rev. B **95**, 174444 (2017); M. Anand, J. Carrey, and V. Banerjee, *ibid.* **94**, 094425 (2016).
[36] T. Orlando, A. Capozzi, E. Umut, L. Bordonali, M. Mariani, P. Galinetto, F. Pineider, C. Innocenti, P. Masala, F. Tabak, M. Scavini, P. Santini, M. Corti, C. Sangregorio, P. Ghigna, and A. Lascialfari, J. Phys. Chem. C **119**, 1224 (2015).
[37] L. Rebbouh, R. P. Hermann, F. Grandjean, T. Hyeon, K. An, A. Amato, and G. J. Long, Phys. Rev. B **76**, 174422 (2007).
[38] A. Bencini and D. Gatteschi, *Electron Paramagnetic Resonance of Exchange Coupled Systems* (Springer-Verlag, Berlin, 1990).
[39] C. Sun, J. S. H. Lee, and M. Zang, Adv. Drug. Delivery Rev. **60**, 1252 (2008).
[40] Y. Yin, R. M. Rioux, C. K. Erdonmez, S. Hughes, G. Somorjai, and A. P. Alivisatos, Science **304**, 711 (2004).
[41] H. J. Fan, U. Gsele, and M. Zacharias, Small **3**, 1660 (2007).
[42] V. Bonanni, M. Basini, D. Peddis, A. Lascialfari, G. Rossi, and P. Torelli, Appl. Phys. Lett. **112**, 022404 (2018).
[43] M. Basini, Effect of the hollow topology on the sin dynamics in iron oxide magnetic nanoparticles, Ph.D. thesis, Università degli Studi di Milano, 2017.
[44] See Supplemental Material at http://link.aps.org/supplemental/10.1103/PhysRevB.102.195424 for sample characterization of size, morphology, and magnetic state.
[45] H. Khurshid, W. Li, V. Tzitzios, and G. C. Hadjipanayis, Nanotechnology **22**, 265605 (2011).
[46] F. Sayed, Hollow magnetic nanoparticles: Experimental and numerical studies, Ph.D. thesis, L'Université du Maine et L'Ecole Doctorale des Sciences et Technologie, 2016.
[47] I. J. Bruvera, P. M. Zelis, M. P. Calatayud, G. F. Goya, and F. H. Sanchez, J. Appl. Phys. **118**, 184304 (2015) .
[48] J. L. Dormann, D. Fiorani, and E. Tronc, in *Advances in Chemical Physics*, Vol. 98, edited by I. Prigogine and S. A. Rice (John Wiley & Sons, Inc., Hoboken, NJ, 1997).
[49] C. Cannas, A. Musinu, G. Piccaluga, D. Fiorani, D. Peddis, H. K. Rasmussen, and S. Mørup, J. Chem. Phys. **125**, 164714 (2006).
[50] X. Batlle and A. Labarta, J. Phys. D: Appl. Phys. **35**, R15 (2002).
[51] J. S. Lord, J. Phys.: Conf. Ser. **17**, 014 (2005).
[52] F. Borsa, A. Lascialfari, and Y. Furukawa, NMR in magnetic molecular rings and clusters, in *Novel NMR and EPR Techniques*, edited by J. Dolinsek, M. Vilfan, and S. Zumer (Springer, Berlin, 2006), pp. 297–349.
[53] T. Moriya, Prog. Theor. Phys. **16**, 23 (1956).
[54] Y. Gossuin, T. Orlando, M. Basini, D. Henrard, A. Lascialfari, C. Mattea, S Stapf, and Q. L. Vuong, Nanotechnology **27**, 155706 (2016).
[55] *NMR-MRI, muSR and Mössbauer Spectroscopies in Molecular Magnets*, edited by P. Carretta and A. Lascialfari (Spinger-Verlag, Berlin, 2007).
[56] E. Shevchenko, M. I. Bodnarchuk, M. V. Kovalenko, D. V. Talapin, R. K. Smith, S. Aloni, and W. A. P. Heiss, Adv. Mater. **20**, 4323 (2008).
[57] A. Cabot, V. F. Puntes, E. Shevchenko, Y. L. Balcells, M. A. Marcus, S. M. Hughes, and A. P. Alivisatos, J. Am. Chem. Soc. **129**, 10358 (2007).
[58] H. Khurshid, W. Li, M. H. Phan, P. Mukherjee, G. C. Hadjipanayis, and H. Srikanth, Appl. Phys. Lett. **101**, 022403 (2012).
[59] G. Hassnain Jaffari, A. Ceylan, C. Ni, and S. Ismat Shah, J. Appl. Phys. **107**, 013910 (2010).
[60] D. Goll, A. E. Berkowitz, and H. N. Bertram, Phys. Rev. B **70**, 184432 (2004).